Deep-Sea Research II 91 (2013) 128–138

Contents lists available at SciVerse ScienceDirect

Deep-Sea Research II

journal homepage: www.elsevier.com/locate/dsr2

Surface vertical PV fluxes and subtropical mode water formation in an eddy-resolving numerical simulation

Guillaume Maze [a,*], Julie Deshayes [a], John Marshall [b], Anne-Marie Tréguier [a], Alexandre Chronis [a], Lukas Vollmer [a]

[a] Ifremer, Laboratoire de Physique des Océans, UMR CNRS 6523, Ifremer, CNRS, IRD, UBO, BP70, 29280 Plouzané, France
[b] Department of Earth, Atmospheric, and Planetary Sciences, Massachusetts Institute of Technology, Cambridge, MA, United States

ARTICLE INFO

Available online 28 February 2013

Keywords:
Subtropical mode water
Potential vorticity flux
Mesoscale turbulence

ABSTRACT

Subtropical mode waters are characterized by low potential vorticity (PV) and so the mechanisms by which PV is extracted from the ocean by air–sea interaction are of great relevance to our understanding of how mode waters are formed. This study analyzes those mechanisms by comparing the magnitude and spatial patterns of surface PV fluxes of diabatic and frictional origin in a high resolution numerical simulation of the North Atlantic. The model resolves mesoscale eddies and exhibits realism in the volume and regional distribution of subtropical mode water, both in the annual-mean and seasonal cycle.

It is found that the diabatic and mechanic fluxes of PV through the sea surface are of similar amplitude locally, but their spatial structures are very different. The diabatic PV flux has a large scale pattern that reflects that of air–sea heat fluxes directed from the ocean to the atmosphere along and to the south of the separated Gulf Stream. In contrast the mechanical PV flux, because of its dependence on horizontal surface density gradients, exhibits much smaller scales but embedded within a coherent large scale pattern. When mapped over the North Atlantic subtropical mode water (EDW) outcropping region, the diabatic PV flux pattern is found to be directed out of the ocean everywhere, whereas the mechanical PV fluxes exhibits small-scale patterns of both sign. The amplitude of the diabatic PV fluxes is found to be at least one order of magnitude larger than the mechanical PV fluxes demonstrating the overwhelming importance of diabatic processes in creating mode waters.

Finally, we note that the large scale climatological patterns and magnitudes of both diabatic and mechanical PV flux mapped over the EDW outcropping region, are very similar to patterns obtained from coarse-grained ocean state estimates that do not resolve the eddy field.

1. Introduction

The ocean contributes to the current climate via the poleward heat transport, which is maximum (and larger than its atmospheric counterpart) in the northern hemisphere tropics, where western boundary currents advect heat northward (e.g. Trenberth and Caron, 2001). In the North Atlantic, heat is transported by the Gulf Stream (hereinafter GS) and then by the North Atlantic Current from subtropical to subpolar and higher latitudes, where it is released to the atmosphere and North Atlantic Deep Water (an essential component of the global Meridional Overturning Circulation) is formed. Nevertheless, a large amount of heat (roughly half of that transported at 26°N, Ganachaud and Wunsch, 2000) is directly transferred to the atmosphere along the path of the Gulf Stream leading to the formation of Eighteen Degree Water (a variety of subtropical mode water, hereinafter EDW).

EDW is characterized by nearly uniform temperature close to 18 °C. It is weakly stratified, typically 250 m thick, and widely spread over the western subtropical North Atlantic. Recent studies used the ocean synthesis OCCA – the synthesis of various observations using the MITgcm (Marshall et al., 1997a, 1997b) as an interpolation tool – to produce a detailed picture of the formation and seasonal cycle of EDW (Forget et al., 2011; Maze and Marshall, 2011; Maze et al., 2009) on a coarse grained, 1° grid. EDW is formed by air–sea heat fluxes in the western part of the subtropical gyre, just south of the Gulf Stream. Formation peaks in February when the EDW layer is thickened by convection. Over the remainder of the year, newly created EDW is consumed by air–sea heat fluxes and ocean mixing, over the entire subtropical gyre. Kwon and Riser (2004) used raw historical observations covering a longer period to estimate interannual fluctuations in

* Corresponding author.
E-mail address: gmaze@ifremer.fr (G. Maze).

0967-0645/$ - see front matter © 2013 Elsevier Ltd. All rights reserved.
http://dx.doi.org/10.1016/j.dsr2.2013.02.026

EDW characteristics. They suggest that EDW properties integrate atmospheric conditions, represented by the North Atlantic Oscillation (hereinafter NAO) index, over times of up to 6 years. Hence EDW can be seen as a reservoir of low potential vorticity. Note that EDW is also a reservoir for CO_2 on interannual time scale (Bates et al., 2002).

At the same time observational programs have been undertaken to describe better the dynamics of EDW (CLIMODE, Marshall et al., 2009) and various model experiments designed to simulate the different processes that influence EDW. Realistic configurations are constrained by the need to capture the separation of the Gulf Stream near Cape Hatteras, which requires a horizontal resolution of at least 1/10° (Bryan et al., 2007). Moreover, mesoscale eddies seem to play a role in the formation and destruction of EDW (see Marshall, 2000; Thomas, 2005; Valdivieso Da Costa et al., 2005, for instance). Given that the first baroclinic Rossby radius of deformation is of the order of 30 km in the region where EDW is formed (Chelton et al., 1998), resolving the mesoscale processes requires a horizontal grid spacing of less than 10 km. It is only quite recently that realistic simulations of the North Atlantic have become available at such horizontal resolution. To our knowledge, the formation of EDW has not yet been studied in these models.

Model simulations of Levy et al. (2010) at very high resolution indicate that sub-mesoscale processes influence the gyre circulation and the dynamics of subtropical mode water. Although this result is presumably highly constrained by the idealized configuration (closed rectangular ocean basin with vertical walls, forced by analytical wind and buoyancy fluxes), it is quite intriguing to compare mode water formation in such a simulation with the picture that arises in simulations with coarser resolution: the classical bowl shape of EDW south of the Gulf Stream (Forget et al., 2011) is largely eroded by sub-mesoscale eddies and confined in between steep isopycnals associated with strong zonal jets. The purpose of this study is to start to bridge the gap between these two extreme perspectives on mode water formation, by analyzing a realistic mesoscale resolving simulation of the subtropical North Atlantic. A second step toward bridging this gap would be to analyze a realistic sub-mesoscale simulation. Ideally, the latter should be fully coupled with the atmosphere in order to resolve asymmetry between upfront and downfront winds under variable fronts, eddies and winds, a level of understanding not accessible with the current simulation used in this study.

Classically, it has been considered that surface buoyancy loss, in particular sensible and latent heat, dominates as the driver for EDW formation. However, winds directed in the downstream direction of intense surface fronts may, for short periods, induce Ekman-driven convection and formation of EDW (Thomas, 2005). This process has only been studied in idealized numerical simulations (Taylor and Ferrari, 2010; Thomas and Ferrari, 2008), while the integrated effect of downfront winds on surface fluxes of potential vorticity in the North Atlantic has thus far only been estimated in coarse resolution data sets (Czaja and Hausmann, 2009; Maze and Marshall, 2011; Olsina et al., 2013) that do not adequately resolve Ekman-driven convection. In this study, we take advantage of having a realistic eddy-resolving simulation of the North Atlantic to evaluate the respective contribution of each driver of EDW formation: buoyancy loss at the surface, referred to as buoyancy forcing, relative to wind stress inducing Ekman-driven convection, referred to as mechanical forcing.

This paper is a contribution to understand better the role of the ocean and its mesoscale in climate. We focus on EDW formation and address two questions: how do mesoscale eddies influence EDW formation? and what is the respective role of buoyancy vs mechanical forcing in EDW formation? We begin in Section 2 by presenting details of the simulation used in this study. In Section 3, we describe the simulated reservoir of EDW during the four seasons by analyzing the 3D potential vorticity field in the region of the Gulf Stream. Then we calculate surface fluxes of potential vorticity and their contribution to EDW formation (Section 4). Finally, we discuss all results (Section 5) and conclude (Section 6).

2. The simulation

2.1. Model and configuration

The model used herein is based on the NEMO framework version 2.3 (Madec, 2008), which combines the free-surface, *z*-coordinate, primitive equation code OPA9 and the multi-layered sea-ice code LIM2 (Fichefet and Morales Maqueda, 1997). This North Atlantic configuration has been developed in the context of the DRAKKAR project (www.ifremer.fr/lpo/drakkar, Barnier et al., 2006). The model grid is based on the ORCA global tri-polar grid (Madec and Imbard, 1996) at 1/12° resolution: the horizontal grid resolution varies from 10 km near the equator to less than 3 km in the northernmost part of the domain, and is about 7.5 km in the Gulf Stream region. The vertical grid contains 64 levels of constant depth; vertical spacing is finer near the surface (6 m) and increases with depth up to 200 m at the bottom. Partial steps are implemented to better represent the bottom topography (Penduff et al., 2007).

The bathymetry of the model, prepared by MERCATOR OCEAN,[1] is a smoothed version of ETOPO2[2] with hand modifications in Gibraltar, Faroe Bank Channel and the Romanche Fracture zone. The model has open boundaries at 80°N and 20°S, where monthly means of DRAKKAR simulation ORCA025-G70 are applied (Barnier et al., 2006). There is radiation only along the southern boundary with a time scale set to 1 day for inflow conditions and to 150 days for outflow conditions. The Mediterranean Sea is only partly included in the model: the eastern boundary of the domain is at 20°E and there is restoring to Levitus et al. (1998) climatology near the boundary.

The model is integrated from rest with temperature and salinity from the Levitus et al. (1998) climatology and sea ice from year 1980 of ORCA025-G70. The atmospheric forcing is DRAKKAR forcing set version 4 (Brodeau et al., 2010) that blends daily satellite-derived radiative fluxes (ISCCP, Zhang et al., 2004, with corrections of CORE data set assembled by W. Large) and monthly precipitations (corrected from CORE) with 6-hourly atmospheric surface variables for turbulent fluxes from the EMCWF reanalysis ERA40. The turbulent fluxes, outgoing radiation and albedo are calculated using the formulae proposed with the CORE data set (Large and Yeager, 2004, 2009). The forcing set was preprocessed and interpolated on the 1/4° ORCA grid; it is linearly interpolated for our 1/12° configuration. Continental runoffs, calculated using Dai and Trenberth (2002), are monthly climatologies. Vertical mixing is increased (up to 1.6×10^{-3} kg m^{-2} s^{-1}) near the largest river outflows. There is relaxation of sea surface salinity to the monthly climatology of Levitus et al. (1998), with a decay time of 180 days for 10 m of water depth.

We use the standard NEMO scheme for penetrative solar radiation based on clear water only (it does not take into account the water color) with a penetration length of 17 m. The simulation is performed with a free surface but constant volume is imposed. Advection scheme is TVD (2nd order centered scheme

[1] http://www.mercator-ocean.fr

[2] ETOPO2v2 Global Gridded 2-minute Database, National Geophysical Data Center, National Oceanic and Atmospheric Administration, U.S. Dept. of Commerce, http://www.ngdc.noaa.gov/mgg/global/etopo2.html.

with corrected flux) for tracers and energy-enstrophy conserving scheme for momentum (Barnier et al., 2006; Le Sommer et al., 2009). Lateral parameterizations include isopycnal Laplacian diffusion of tracers with a coefficient that decreases linearly as a function of grid size from 100 $m^2\ s^{-1}$ at the equator to 20 $m^2\ s^{-1}$ at the pole. There is also biharmonic diffusion of momentum with coefficient A_ν that decreases from the equator, where $A_\nu = 1.25\times 10^{10}\ m^4\ s^{-1}$, toward the pole at the third power of the grid size. The parametrization of vertical physics is achieved with a turbulent kinetic energy (hereinafter TKE) closure plus an enhanced vertical mixing of tracers and momentum in case of static instability. In addition, a quadratic bottom friction and no-slip lateral boundary conditions (excepted in the subpolar gyre) are used.

The complete simulation covers the period 1980–2006. All the diagnostics performed in this paper are based on 5-day average outputs for the period ranging from January 2003 to December 2006. We thus cover 4 complete years and seasonal cycles. This choice is motivated by our desire to directly compare results presented here with those obtained using the OCCA data set (Forget, 2010; Maze and Marshall, 2011; Maze et al., 2009) which covers the same period. Because OCCA has a horizontal resolution of $1^\circ\times 1^\circ$ it does not explicitly simulate mesoscale eddies. However, it is constrained to closely fit surface altimetry, SST and the Argo data over the analysis period. Comparing our analysis using the NATL12 simulation with those of the aforementioned studies will allow us to identify the specific roles of mesoscale eddies in the EDW formation process. In particular we will focus on quantifying the relative role of mechanical versus thermodynamic PV forcing in EDW formation.

2.2. Simulated circulation and EDW layer

The simulation realistically reproduces the subtropical North Atlantic circulation: the subtropical gyre circulation is 73 Sv (maximum of the barotropic streamfunction) on average over the period 2003–2006, the Gulf Stream separates from the coast at about 37.5°N and surface eddy kinetic energy reaches up to 2000 $cm^2\ s^{-1}$ near the Gulf Stream (color shading in Fig. 1, plot A).

The water mass transformation due to surface buoyancy forcing is analyzed over the whole domain using the Walin framework (see details of the method in Maze et al., 2009). The 2003–2006 mean transformation rate as a function of surface

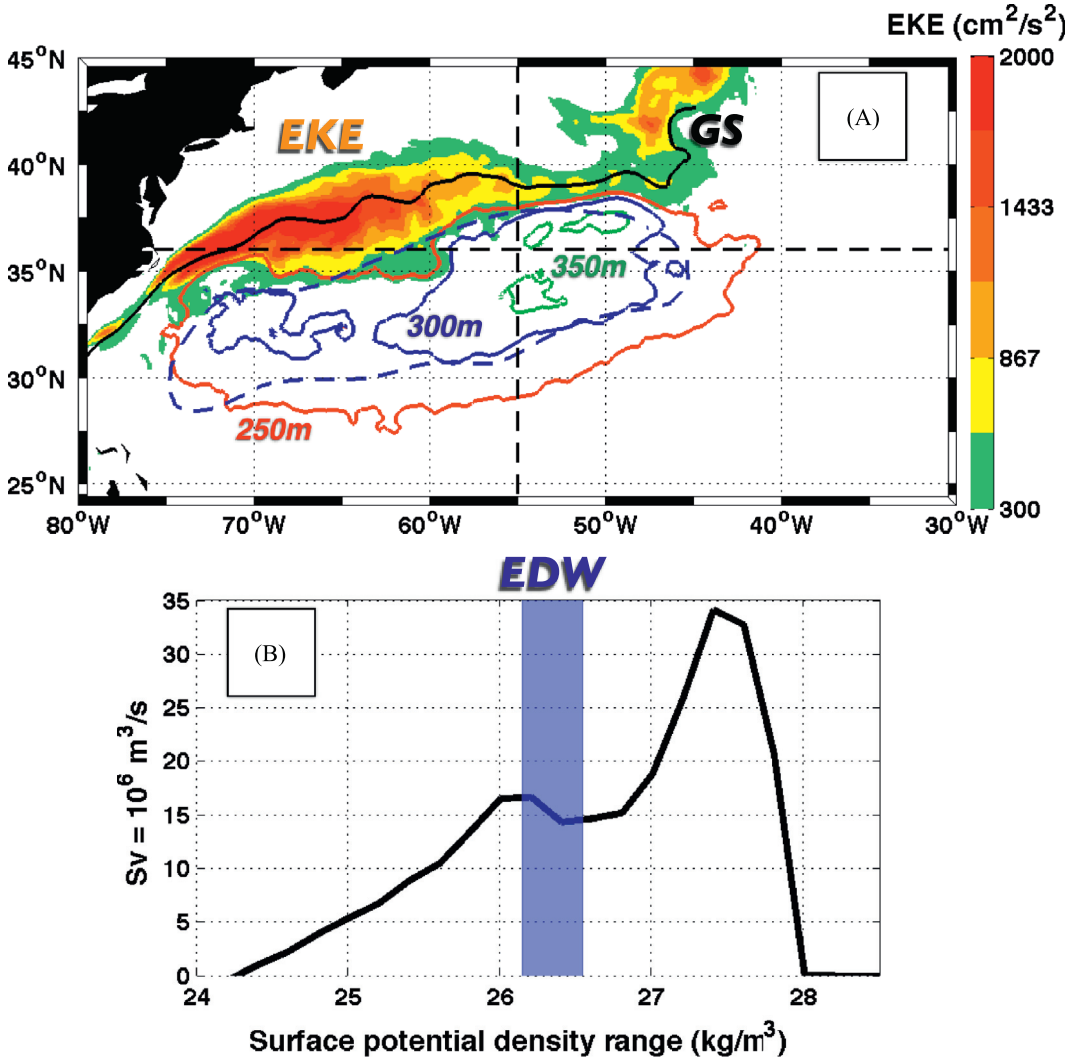

Fig. 1. Panel A: Solid colored contours are 2003–2006 mean EDW thickness (250, 300 and 350 m) from the mesoscale eddy resolving simulation NATL12 (the OCCA data set, Forget, 2010, equivalent 300 m thickness contour is shown by the dashed blue contour). The thick black line is the 17 °C isotherm mean position at 200 m depth, indicative of the Gulf Stream location. The color shading is the surface mean Eddy Kinetic Energy (EKE), see colorbar for amplitude in $cm^2\ s^{-1}$. Dashed black lines localize the meridional section at 55°W and zonal section at 36°N shown in Figs. 2 and 3. Panel B: The 2003–2006 mean water mass transformation rate (in $S\nu = 10^6\ m^3\ s^{-1}$) due to surface buoyancy fluxes per density classes (see details of the method in Maze et al., 2009). The subtropical mode water density range $\sigma_{EDW} = 26.34 \pm 0.2\ kg\ m^{-3}$ is highlighted by the blue shaded band.

potential density class is shown in Fig. 1, plot B. A positive transformation rate corresponds to a volume flux across the isopycnal surface from lighter to heavier densities (thus primarily northward). For the potential density layer 26.34 ± 0.2 kg m^{-3} (highlighted in blue), there is a convergence of volume fluxes because transformation is larger across the warm flank than across the cold one. This convergence corresponds to the formation of about 4 Sv of subtropical mode water by surface buoyancy forcing, a figure in line with bibliographical standards and error estimates of the method (Forget et al., 2011; Maze et al., 2009). We also found the model to reproduce a realistic seasonal cycle of the water mass transformation rates (not shown) when compared with estimates in Maze et al. (2009).

Combining this information with the analysis of summer time vertical sections across the subtropical gyre of potential density and potential vorticity (see next section) we determined the core potential density of subtropical mode water to be $\sigma_{EDW} = 26.34$ kg m^{-3} with a density range of $\sigma_{EDW} \pm 0.2$ kg m^{-3}. Those properties are consistent with observations (Forget et al., 2011; Kwon and Riser, 2004).

Using this definition, with no restriction on stratification, the 2003–2006 time average thickness of EDW is computed. It is shown as colored contours in Fig. 1, plot A. The EDW has an annual mean maximum thickness of about 350 m between 50W and 55W at 36N. It is stored in two main reservoirs south of the Gulf Stream: one centered around 52W, the other around 70W, very similar to that found in observations (Kwon and Riser, 2004). Significant volumes are observed down to 30N. The NATL12 EDW 300 m thickness contour (blue) follows that of the OCCA data set (dashed blue contour in Fig. 1A) although the separation between the two EDW reservoirs is less clear in OCCA. This is probably due to the more intense eddy kinetic energy (EKE) in NATL12 which clearly seems to delineate the EDW reservoir (see next section).

The annual mean EDW volume is 57 Sv y where 1 Sv y $\simeq 3.15 \times 10^{13}$ m^3 corresponds to a flow of 1 Sv $= 10^6$ m^3 s^{-1} sustained over 1 year. The amplitude of the seasonal cycle of EDW volume is about 11 Svy with a maximum at the end of March. No significant accumulation or destruction of EDW was found over the analyzed period. These volumes are consistent with state of the art references such as those discussed at length in Forget et al. (2011).

3. Eighteen degree water potential vorticity seasonal cycle

In this section we describe the EDW seasonal cycle of planetary potential vorticity, hereinafter PPV (following previous studies, Maze and Marshall, 2011) defined by

$$\mathrm{PPV} = -\frac{f}{\rho}\frac{\partial \sigma}{\partial z} \tag{1}$$

where f is the Coriolis parameter, ρ the *in situ* density and σ the potential density.[3] Meridional and zonal PPV sections are plotted in Figs. 2 and 3 for characteristic months of a typical seasonal cycle – December 2005 and March, June and September 2006. The PPV projected on the EDW core isopycnal surface σ_{EDW} is also shown in Fig. 4 so that we have a complete three dimensional perspective of the EDW seasonal cycle. These should be compared with ocean state estimates from OCCA (Figs. 3–5) in Maze and Marshall (2011).

In December (plots A) the EDW core is trapped below the seasonal thermocline and has an annual PPV maximum value. This is simply because it has been isolated from air–sea interactions and ventilation since the previous winter. The mixed layer depth (green curve) – about 100 m south of the GS – is deepening at this time primarily because of buoyancy loss to the atmosphere. The EDW surface outcrop remains far away from the formation region. In March (plots B), the surface outcrops open up and the warmer flank of the EDW migrates sufficiently southwestward to allow the EDW core to be directly ventilated in the mixed layer, which indeed penetrates the EDW core to about 300 m. As can be seen on the zonal section (Fig. 3), the outcrop is open wide from 60W to about 40W at 36N. This is the time when previously existing EDW has its PPV level reset and new EDW is ventilated. In June (plots C), the EDW core is again trapped below the seasonal thermocline. In September (plots D), note that the accumulated effect of mixing processes since the end of the winter has increased the overall PPV values of the layer.

Study of Maze and Marshall (2011) presented exactly the same figures using the OCCA data set which has a significantly lower resolution of 1° – and thus does not explicitly represent mesoscale eddies (Forget, 2010). However, it is constrained to be consistent with Argo and altimetric data. It is therefore interesting to compare those set of figures with the present ones. It is striking to note that the meridional sections are very similar. Both show a characteristic large scale structure in which a pool of low PPV EDW is clearly identified, trapped between the seasonal and permanent thermoclines to the south of the Gulf Stream. Subtropical mode water has long been known to have such a distribution, as far back as its initial discovery in the 1877 Challenger voyage (see Fig. 2 in Worthington, 1959, for instance). Here we show that at high resolution – 1/12° i.e. 7.5 km in the region of interest – this EDW meridional structure is retained, albeit with the imprint of eddies superimposed.

Mesoscale structures are clearly evident in Figs. 3 and 4. The zonal section shows how Gulf Stream meanders west of 60W can isolate a smaller pool of EDW from the principal ventilation region localized further east. These eddy structures are remarkably persistent in time. For instance, at 70W a low PPV core of EDW persists at a depth of about 300 m all year long (see Fig. 3). This seems to be a robust feature as the 2003–2006 average EDW thickness (Fig. 1) shows a secondary reservoir of EDW just south of the GS at 70 W. In fact one can note that the eastern tip of the maximum EKE region – 65 W – coincides with an anomalously thin EDW region south of the Gulf Stream. From the EDW formation perspective, the secondary reservoir of EDW at 70W is clearly not the most ventilated one (see PPV levels in Fig. 4). Hence it may coincide with a region of EDW accumulation due to the recirculation of EDW formed to the east (see the EDW circulation using Bernoulli function contours in Maze and Marshall, 2011). Furthermore, EDW formed locally at 70W seems to be warmer and lighter (consistent with recent CLIMODE observations, see this issue).

The imprint of the mesoscale is also observed all along the outcropping region (see Fig. 4 plot B for instance) from 60 W eastward. As in the coarse OCCA data set, the EDW outcrop (in the range $\sigma_{EDW} \pm 0.2$) is large in March because the EDW warm flank migrates southwestward while the cold flank remains further east.[4] However, in OCCA the PPV distribution over the outcrop is rather uniform and smooth, whereas here the mesoscale imprint on the outcrop PPV distribution is evident. We now consider those air–sea interaction processes that create the low PPV mode water.

[3] Defined as $\sigma = \rho|_{p_{atm}} - 1000$ kg m^{-3}; and usually referred to as σ_θ in the literature.

[4] Note that the southwestward migration of the EDW warm flank reaches 75 W in OCCA and only 60 W in NATL12, because it is more constrained by the GS meanders, as revealed by the EKE pattern.

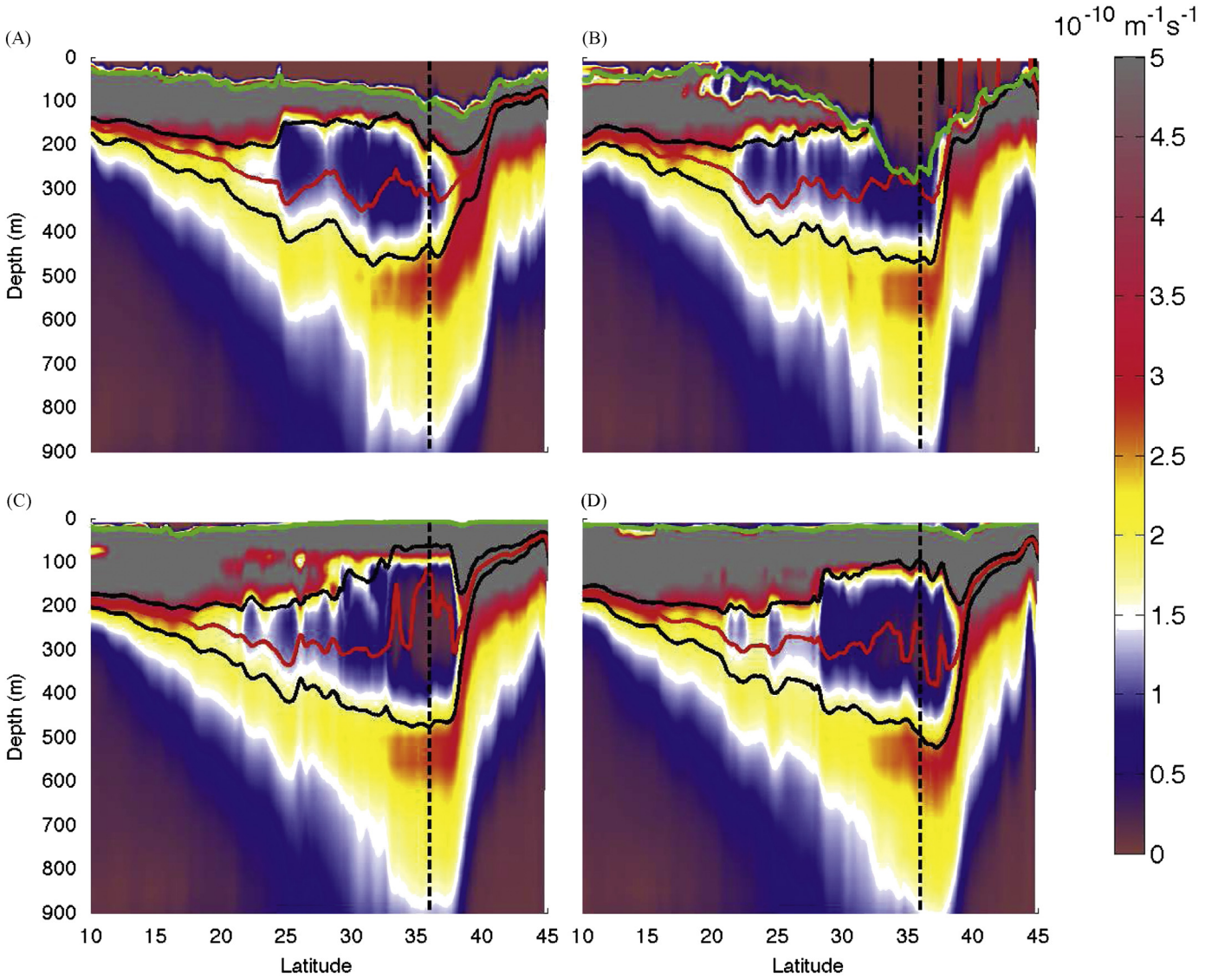

Fig. 2. Meridional section along 55°W (see Fig. 1) of the monthly mean planetary potential vorticity PPV given by Eg. (1) (color shading, note that values greater than 5×10^{10} m^{-1} s^{-1} are saturated in gray). The EDW isopycnal core $\sigma_{EDW} = 26.34$ kg m^{-3} is shown in red while EDW isopycnals layer $\sigma_{EDW} \pm 0.2$ kg m^{-3} are shown in black. Mixed layer depth is plotted as the green contour. The position of the zonal section from Fig. 3 is shown as a thin black dashed vertical line. Monthly mean fields are shown for (A) December 2005, (B) March 2006, (C) June 2006 and (D) September 2006.

4. Surface PV fluxes

EDW formation is fundamentally the process by which an isopycnal layer has its potential vorticity reduced. According to the impermeability theorem there can be no flux of PV through σ surfaces (Haynes and McIntyre, 1987) and so the PV of an isopycnal layer can only be reduced by frictional and buoyancy fluxes acting where the layer outcrops at the sea surface. In this section we thus analyze surface PV fluxes in order to determine where the EDW is formed and what are the relative contributions of mechanical and buoyancy fluxes to the process.

4.1. Theoretical background

A detailed analysis of the potential vorticity flux framework can be found in Marshall and Nurser (1992) and Marshall et al. (2001). Specific discussions of surface PV fluxes with regard to mode waters can also be found in Czaja and Hausmann (2009), Maze and Marshall (2011) and Olsina et al. (2013). Here we assume that the reader is familiar with the equation of PV conservation in its flux form and we therefore only briefly review key formulae. The issues are subtle and reader is referred to the aforementioned studies for more theoretical details.

Very generally the mass weighted Ertel PV is changed by the divergence of a PV flux thus,

$$\frac{\partial \rho Q}{\partial t} = -\nabla \cdot \mathbf{J}$$

where the flux vector $\mathbf{J}$ is given by

$$\mathbf{J} = \rho Q \mathbf{u} + \boldsymbol{\omega} \frac{D\sigma}{Dt} + \mathbf{F} \times \nabla \sigma \tag{2}$$

and ρ is the in situ density, $Q = -\rho^{-1} \omega \cdot \nabla \sigma$ is the Ertel PV, $\boldsymbol{\omega}$ is the absolute vorticity, $\mathbf{u}$ the fluid velocity, D/Dt is the Lagrangian derivative and $\mathbf{F}$ is the (non-conservative) frictional force per unit mass acting in the Boussinesq momentum equation. Note that in Eq. (2) we have neglected the non-advective thermobaric term. Discussed at length in Marshall et al. (2001), this term makes a negligible contribution near the sea surface and is thus ignored here.

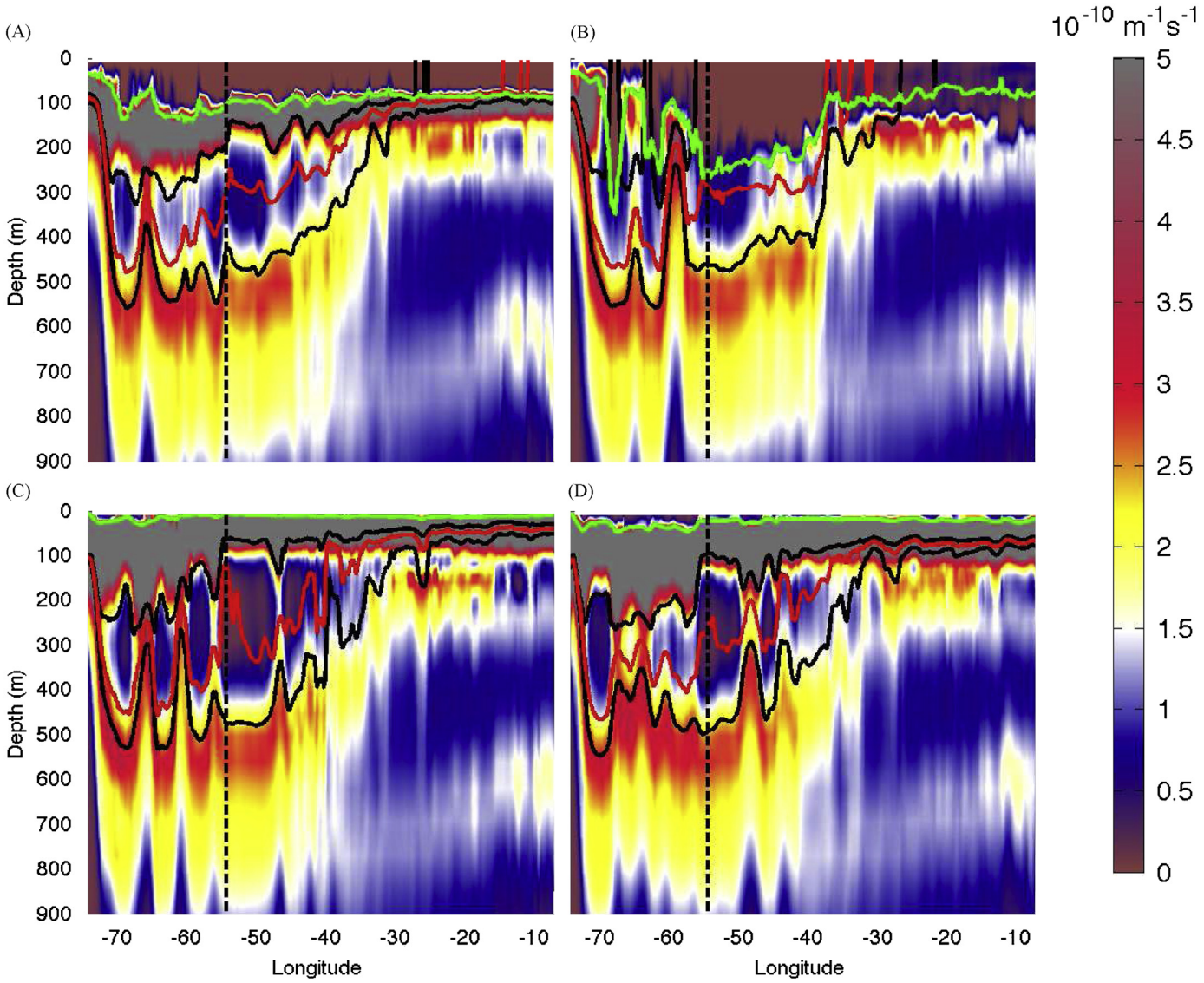

Fig. 3. Same as Fig. 2 but for a zonal section along 36°N. (A) December 2005, (B) March 2006, (C) June 2006 and (D) September 2006.

The PV flux component relevant to the ventilation/formation of mode water is the vertical flux of potential vorticity through the mixed layer. We therefore compute the vertical component of the PV flux averaged over the depth of the mixed layer thus

$$J_s = \frac{1}{h}\int_{-h}^{0} \mathbf{J}\cdot\mathbf{k}\, dz$$

$$J_s = \underbrace{\frac{1}{h}\int_{-h}^{0} f\frac{D\sigma}{Dt}dz}_{diabatic} + \underbrace{\frac{1}{h}\int_{-h}^{0}(\mathbf{F}\times\nabla\sigma)\cdot\mathbf{k}\, dz}_{mechanical} \quad (3)$$

where h is the mixed layer depth (variable in time) and $\mathbf{k}$ the local vertical unit vector. The first and second terms on the r.h.s. of Eq. (3) will be referred to as J_s^{diab} and J_s^{mech}, representing contributions from buoyancy and mechanical forcing, respectively. We note that a positive vertical PV flux is directed from the ocean to the atmosphere and corresponds to an oceanic loss of PV inducing mixing and reducing stratification.

The diabatic contribution can be evaluated by setting $D\sigma/Dt$ equal to the vertical divergence of non-advective buoyancy flux, multiplying by f and integrating over the mixed layer. This yields the following expression comprising contributions from the air–sea buoyancy flux and entrainment fluxes at the base of the mixed layer:

$$J_s^{diab} \simeq -\frac{f}{h}\left(\frac{\alpha Q_{net}}{C_w} - \rho_0\beta S_{net} + w_{ent}\Delta\sigma\right) \quad (4)$$

where Q_{net} is the sea-surface net heat flux (negative indicating cooling of the ocean and where short wave radiative fluxes include only those that diverge in the mixed layer), α is the thermal expansion coefficient, C_w is the specific heat of seawater, β is the haline expansion coefficient, S_{net} is the net fresh water flux (positive if evaporation exceeds precipitation), w_{ent} is the entrainment velocity at the base of the mixed layer and $\Delta\sigma$ is the potential density jump across the base of the mixed layer.

In a similar manner, writing the frictional force $\mathbf{F}$ as

$$\mathbf{F} = \frac{1}{\rho_0}\frac{\partial\boldsymbol{\tau}}{\partial z} \quad (5)$$

where ρ_0 is a reference density and $\boldsymbol{\tau}$ represents the vertical transport of horizontal momentum by small-scale processes expressed as a turbulent stress, substituting Eq. (5) into J_s^{mech} yields

$$J_s^{mech} = \frac{1}{\rho_0 h}\int_{-h}^{0}\left(\frac{\partial\boldsymbol{\tau}}{\partial z}\times\nabla\sigma\right)\cdot\mathbf{k}$$

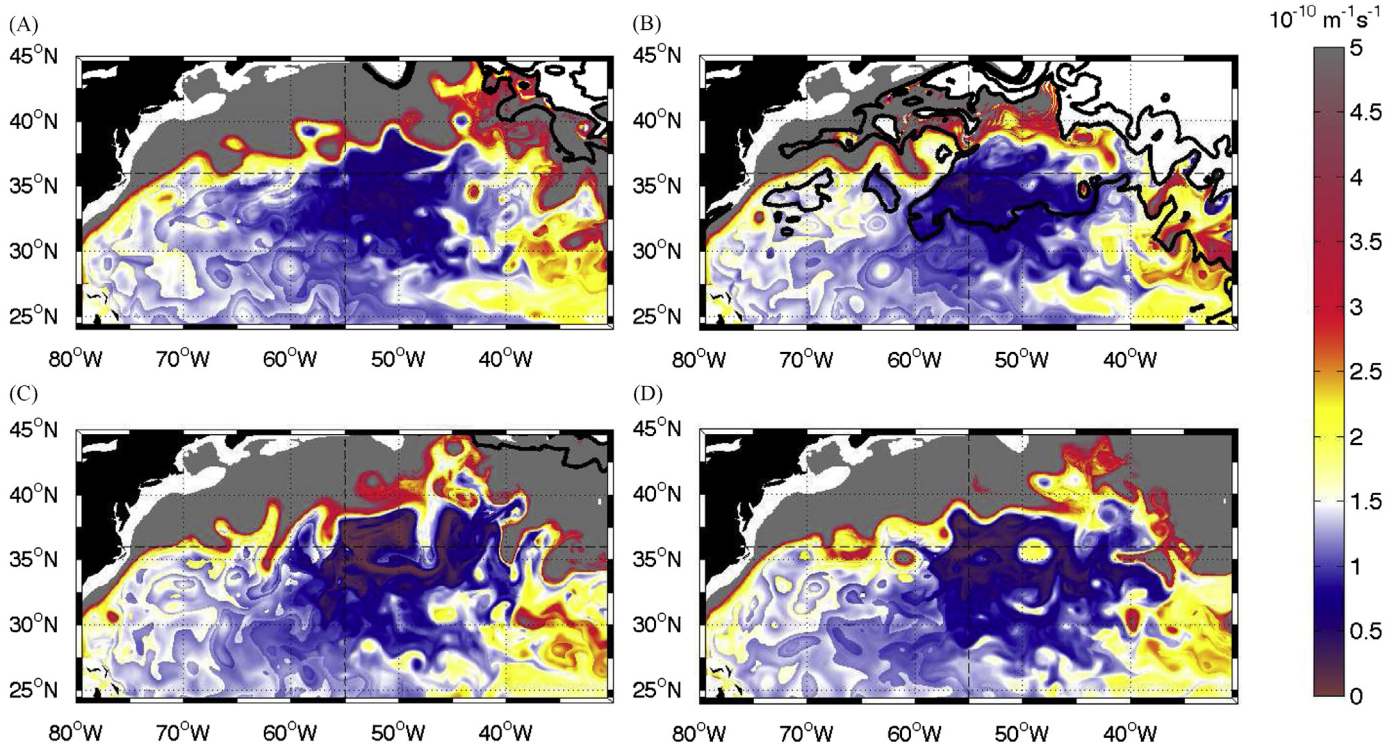

Fig. 4. Color shading: monthly mean planetary potential vorticity projected on the $\sigma_{EDW} = 26.34\ \mathrm{kg\ m^{-3}}$ EDW core isopycnal surface. Thick black contours: $\sigma = 26.34 \pm 0.2\ \mathrm{kg\ m^{-3}}$ outcrops at the surface. Monthly mean fields are plotted for December 2005 (panel A) and March (panel B), June (panel C) and September (panel D) 2006. Light dashed black lines indicate the meridional section at 55°W and zonal section at 36°N shown in Figs. 2 and 3. (A) December 2005, (B) March 2006, (C) June 2006 and (D) September 2006.

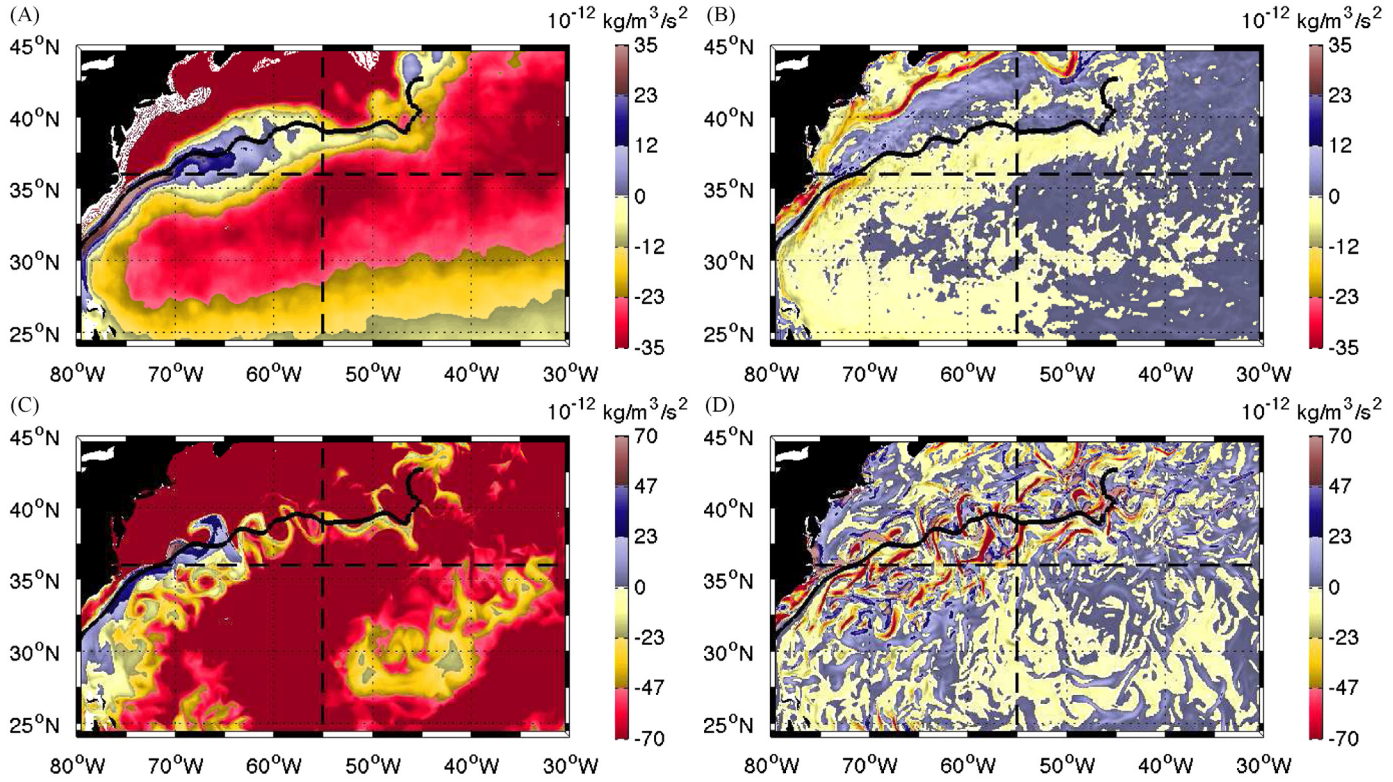

Fig. 5. Upper plots: spatial distribution of time-mean (2003–2006) local PV fluxes. (A) Diabatic flux J_s^{diab} from Eq. (4) and (B) mechanical flux J_s^{mech} from Eq. (6). Lower plots: daily mean snapshots of J_s^{diab} (panel C) and J_s^{mech} (panel D) for 2003 June 24th. Thick black line is the Gulf Stream position. Light dashed black lines indicate the meridional section at 55°W and zonal section at 36°N shown in Figs. 2 and 3. (A) 2003–2006 mean of local J_z^{diab}, (B) 2003–2006 mean of J_z^{mech}, (C) 2003/6/24 snapshot of local J_z^{diab} and (D) 2003/6/24 snapshot of local J_z^{mech}.

$$J_s^{mech} = \left(\frac{\boldsymbol{\tau}_s}{\rho_0 h} \times \nabla\sigma\right) \cdot \mathbf{k} dz \tag{6}$$

where $\boldsymbol{\tau}_s$ is the (wind) stress at the surface and we have assumed that the stress at the base of the mixed layer is vanishingly small and that the potential density is constant over the mixed layer. The above formulations of diabatic equation (4) and mechanic equation (6) PV fluxes are those, for example, used by Czaja and Hausmann (2009).

We now wish to compute and map equations (4) and (6) over the EDW outcrop as it seasonally migrates, enabling us to isolate specific times and locations when the EDW core layer is ventilated (Maze and Marshall, 2011). To carry out this Lagrangian (outcrop-following) technique, we define a time series and a mean map of PV flux experienced by the EDW low PV layer as in Maze and Marshall (2011):

$$\mathcal{J}_s(X_i,h) = \int_{X_j} J_s(t,x,y)\mathcal{H}_h^{zref}(t,x,y)\, dX_j \tag{7}$$

where (t,x,y) are the time-, zonal- and meridional-axis. A time series (a spatial average) is obtained by setting $X_i = t$ and $X_j = (x,y)$; and a two dimensional map (average in time) is obtained by setting $X_i = (x,y)$ and $X_j = t$. Here $\mathcal{H}$ is the outcrop mapping function given by

$$\mathcal{H}_h^{zref}(t,x,y) = \begin{cases} 1 & \text{if} \begin{cases} \sigma_{EDW} - \dfrac{\delta\sigma}{2} < \sigma_s \\ \sigma_s \le \sigma_{EDW} + \dfrac{\delta\sigma}{2} \\ \mathrm{h} \ge z_{ref} \end{cases} \\ 0 & \text{otherwise} \end{cases} \tag{8}$$

This is a binary function which takes a value of unity when the surface potential density is in the EDW outcrop range $\sigma_{EDW} \pm \delta\sigma$ and has a mixed layer depth deeper than a reference depth z_{ref}, and is zero otherwise. Note that this mapping function does not discriminate against times when PV fluxes are negative.

The reference depth z_{ref} is chosen to be deeper than that of the seasonal thermocline which in summer overlies the EDW core region. Examination of Fig. 2, panel C, suggests that setting $z_{ref} = 100$ m is reasonable and is the same value used by Maze and Marshall (2011). This z_{ref} criterion ensures that our mapping is restricted to times when the surface outcrop is in direct contact with the EDW low PV reservoir. This is equivalent to restricting the mapping to regions where the – mostly meridional – seasonal migration of EDW isopycnal surfaces are relatively small (see Fig. 2 in Maze and Marshall, 2011).

In the following sections we will describe local mean PV flux patterns and then use the Lagrangian mapping technique to describe PV fluxes associated with the cycle of EDW formation and loss.

4.2. Local vertical PV fluxes

The 2003–2006 time mean and a daily snapshot (2003, June 24th) of local diabatic (Eq. (4)) and mechanical (Eq. (6)) PV fluxes through the sea surface are shown in Fig. 5. The 2003–2006 time mean of the diabatic PV flux (Fig. 5, panel A) is predominantly negative (i.e. into the ocean). South of the GS, over most of the subtropical gyre, diabatic fluxes are about -30×10^{-12} kg m^{-3} s^{-2}. North of the GS, diabatic fluxes are much more intense with values smaller than -70×10^{-12} kg m^{-3} s^{-2}. These areas of negative diabatic PV fluxes are driven by summer time buoyancy gain which, weighted by a shallow seasonal mixed layer, compensate more than the large winter time buoyancy loss over the seasonal cycle. It is interesting to note that the diabatic PV flux depends on Q_{net}/h. Therefore even if winter and summer time buoyancy fluxes tend to almost balance each other over a seasonal cycle, the related PV flux does not, because of the large difference of mixed layer depth between summer and winter. However, all along the GS (denoted as a black line in Fig. 5) we observe positive diabatic PV fluxes with values off the American coast larger than 50×10^{-12} kg m^{-3} s^{-2}. This is due to the fact that the GS loses buoyancy all year long as it carries warm waters northward that are never in thermal balance with the overlying atmosphere.

The 2003–2006 time mean of local mechanical PV flux (Fig. 5, panel B) has a more complex pattern than the diabatic one because it involves the cross product of the wind stress with the surface density field gradient in a lateral Ekman heat flux manner (see Eq. (6)). Large density fronts around eddies induce intense local mechanical PV fluxes of both signs. On panels C and D of Fig. 5 are shown daily snapshots for 2003 June 24th of the diabatic and mechanical PV fluxes. In the region of the GS, frequent occurrence of large density fronts around eddies induce positive and negative mechanical PV fluxes of the same absolute order of magnitude as the diabatic PV flux. However, over a longer period, large but small scale and opposite signs mechanical PV fluxes tend to average out. As can be seen on the 2003–2006 time mean (Fig. 5, panel B) the local mechanical PV flux has very localized mesoscale features.

Because the wind stress is predominantly eastward over this region, the J_s^{mech} mean pattern can be understood considering the surface density front structure alone. We will describe it starting from the coast moving eastward into the open ocean. First, on the American continental shelf fresh waters (Fratantoni and Pickart, 2007) when advected into the open ocean increase the stratification and induce negative PV fluxes (this is the first yellow band area on panel B). Second, north of Cape Hatteras where the GS detaches from the coast, westerlies bring cold waters of the subpolar recirculation on top of warmer waters which triggers convection and PV loss, a positive PV flux (first large blue area). Third, westerlies bring the anomalously warm waters of the GS over the colder waters of the subtropical gyre which increases the stratification and induces a negative PV flux (second yellow band). Between 30°N and 36°N the previous three patterns persist and are particularly close to each other because of the strong zonal density gradients associated with the GS (note that surface cold waters in this region are not from the subpolar recirculation but presumably a result of coastal upwelling). Fourth and last, the cold waters being ventilated south of the GS by deep mixed layers in the winter time are carried southward by westerlies over the warm core of the subtropical gyre inducing a PV loss (second blue band from 70°W eastward).

4.3. Accumulated effects of vertical PV fluxes on EDW

Having described the local PV fluxes, we now investigate how these patterns are modified when mapped for the EDW core ventilation times and locations. Results from diabatic and mechanical PV fluxes using Eq. (7) are shown in Fig. 6, panels A and B. The diabatic PV flux mapped over the EDW outcrop is fundamentally different from the local flux. Because the mapping technique primarily selects winter time EDW core ventilation locations (because of the mixed layer depth criteria over the surface outcrop), the flux is predominantly positive (buoyancy loss) with values larger than 1×10^{-12} kg m^{-3} s^{-2}. This indicates an EDW PV reduction by buoyancy fluxes at the surface, as expected. South of the GS, the diabatic PV flux is the largest east of 60°W on top of the EDW core layer (see the 300 m thickness red contour), which confirms the vertical one-dimensional nature of this water mass formation process.

In contrast, the mechanical EDW core PV flux map (Fig. 6, panel B) does reflect the large scale pattern of the local PV flux,

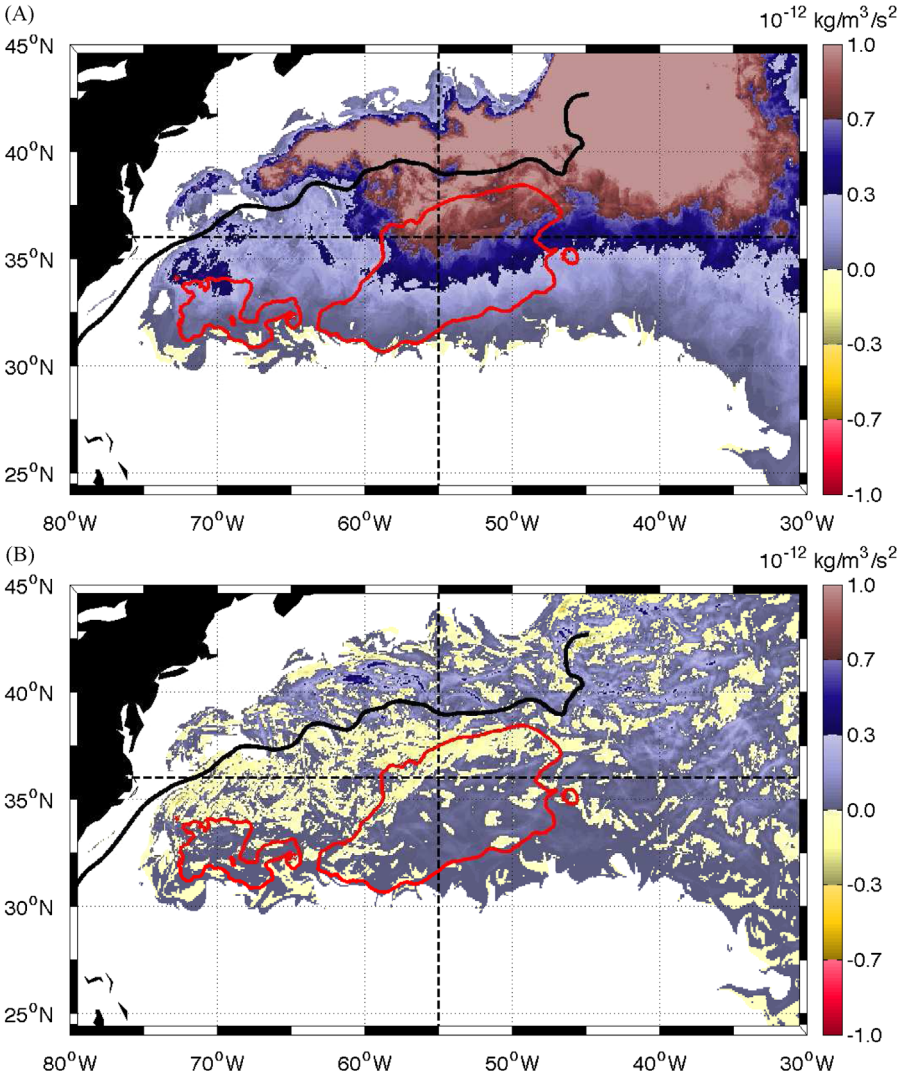

Fig. 6. Time-mean (2003–2006) PV fluxes over the EDW outcrop defined using Eq. (7). (A) Diabatic flux $\mathcal{J}_s^{diab}$ and (B) mechanical flux $\mathcal{J}_s^{mech}$. Thick black line is the Gulf Stream position. Light dashed black lines indicate the meridional section at 55°W and zonal section at 36°N shown in Figs. 2 and 3. Also plotted in red is the 300 m EDW mean thickness contour. (A) 2003–2006 mean EDW J_z^{diab} and (B) 2003–2006 mean EDW J_z^{mech}.

although the mesoscale eddy signature is more visible than for diabatic fluxes. The PV of the EDW core is reduced by positive PV fluxes located (i) on the northern flank of the GS and (ii) south of the GS but never closer to the GS than 2 degrees of latitude. In between these two EDW formation regions lies a destruction area, on the southern flank of the GS. These results bring new details about the EDW formation by mechanical forcing. They are not in contradiction with Ekman-driven convection driving EDW formation along the Gulf Stream. Nevertheless, the picture is more complex than described when considering the GS as a straight zonal density front. Westerlies do not drive cold north-of-the-GS waters southward across the GS to form mode waters south of it. Instead the process more resembles a tongue of GS core water that is warmer and lighter than the surroundings. Therefore on the southern GS flank, light waters from the GS warm core are advected further south, hence increasing the upper ocean PV (the yellow area observed in Fig. 6, panel B). However, EDW mode water is formed along the northern flank of the GS. It is probable that a fraction of it subducts and circulates across the GS to join the EDW pool located south of the GS, as suggested by observations (Thomas and Joyce, 2010; Thomas et al., 2013).

Although the spatial patterns of EDW core diabatic and mechanical PV flux are very different, we can still compare their local amplitudes. Wherever the mechanical PV fluxes are positive, they are one order of magnitude smaller than the diabatic PV fluxes (which are positive everywhere). This is mostly visible north of the GS, where mechanical PV fluxes are of the order of 0.3×10^{-12} kg m^{-3} s^{-2} while diabatic PV fluxes exceed 1×10^{-12} kg m^{-3} s^{-2}. Hence the role of frictional forcing for EDW formation is significant but much smaller than that of buoyancy forcing.

We now compare these results with diagnostics from non-eddy resolving data sets such as OCCA. Diabatic EDW core PV fluxes have a similar pattern and slightly larger amplitude than those in the OCCA data set (see Fig. 7, panel C in Maze and Marshall, 2011), which suggests that mesoscale eddies do not significantly influence the location where buoyancy fluxes form EDW, although they enhance the amplitude. The large scale pattern of mechanical EDW core PV flux is also comparable to the equivalent one from the OCCA data set (see Fig. 8, panel A in Maze and Marshall, 2011). The amplitude of mechanical EDW core PV flux seems slightly smaller than in the OCCA data set, but the net annual fluxes integrated over the North Atlantic are comparable: 0.5×10^7 kg m^{-1} s^{-1} in the present eddy-resolving simulation vs 0.6×10^7 kg m^{-1} s^{-1} in the OCCA data set (Maze and Marshall, 2011). Hence mesoscale eddies do not significantly

influence the (large-scale) location nor the amplitude of mechanical forcing of EDW formation. This result may seem counter-intuitive as the number and intensity of density fronts is expected to be much larger in an eddy-resolving simulation than in a non-eddy resolving data set (although stronger gradients would imply smaller surface areas over which fluxes can act). It suggests that besides Ekman-driven convection that extracts PV from the ocean, there are other mesoscale processes that, in the meanwhile, re-stratify the upper ocean and inhibit Ekman-driven convection.

5. Discussion

This study uses a realistic simulation of the North Atlantic circulation that explicitly resolves mesoscale eddies. By comparing with similar results from coarse resolution ocean state estimates, we focus on the specific role of mesoscale eddies in the EDW formation process. Before going on to our conclusions we discuss our results in the light of limitations in the simulated circulation.

Our simulation at 1/12° horizontal resolution has a grid size of 7.5 km in the Gulf Stream area, which allows one to resolve mesoscale processes. The region of maximum EKE, which follows the path of the Gulf stream from 75W to 65W, is very similar to that found in observations (from satellite altimetry, not shown, and from surface floats, Reverdin et al., 2003). The amplitude, though, is somewhat underestimated: maximum values are of the order of 2000 $cm^2\ s^{-1}$ in the simulation while it exceeds 2500 $cm^2\ s^{-1}$ in observations. Two possible reasons are (i) the lack of turbulent processes on the sub-grid scale, i.e. sub-mesoscale processes, and (ii) a parametrization of the surface turbulent stress as a function of the difference in surface winds and surface currents (Eden and Dietze, 2009). Nevertheless, the large scale structure of the circulation and the thermohaline properties of the upper ocean are much more realistic in the region of the Gulf Stream than a companion lower-resolution simulation ORCA025-G70 that is only eddy-permitting (1/4° resolution). To our knowledge, our current study is the first to investigate the role of mesoscale eddies in EDW formation using a realistic numerical simulation of 1/12° of resolution.

The GS region is an important site of air–sea interaction, and may be the center of action by which the ocean influences NAO fluctuations (Czaja and Frankignoul, 2002; Frankignoul and Kestenare, 2005). The possibility that atmospheric anomalies influenced by the ocean have a local feedback on air–sea PV fluxes and hence EDW formation, cannot be excluded. If such atmospheric anomalies are not present in the forcing set employed, then the result of this feedback will be absent in our calculations. Moreover, it is important to keep in mind that using bulk formulae to force the ocean model implies a spurious damping effect on simulated SST anomalies (compared to forcing with heat fluxes in particular). Whether this damping alters EDW formation processes remains an open question. Coupling our eddy-resolving ocean model with an atmospheric model seems to be the only way forward to answer such questions.

The ocean simulation used here does not resolve sub-mesoscale processes, nor are they parametrized. Idealized simulations of Levy et al. (2010) suggest that there is a dramatic change in the shape of subtropical mode water on progressing from mesoscale resolving (in their case 1/9°) to sub-mesoscale resolving (1/54°) simulations, presumably due to the development of very intense zonal jets. Whether those jets would exist in a realistic configuration (with realistic topography and atmospheric forcings) remains unclear; they are definitely not present in our simulation. In addition, sub-mesoscale processes are likely responsible for additional re-stratification effects that are missing here (Boccaletti et al., 2007; Fox-Kemper et al., 2008). Moreover, coupled processes between variable fronts, eddies and winds are likely to be affected by the presence of sub-mesoscale features, which remains to be quantified in a realistic EDW context. Finally, it should be remembered that the objective of this study is to describe EDW formation in a realistic mesoscale resolving simulation. We are fully aware that sub-mesoscale processes, which are not represented in this simulation, may affect this description. For instance, it is probable that Ekman-driven convection mostly acts on sub-mesoscale fronts. As those are not present in the simulation, we may underestimate the role of Ekman-driven convection in EDW formation (Thomas et al., 2013). Hence our estimate of the relative contribution of the mechanical PV flux contribution to the total PV flux leading to EDW formation will have to be reconsidered as the resolution of our models increases.

6. Conclusion

Recent studies have described in detail the formation of EDW in coarse resolution data sets (either OCCA or Argo, see Czaja and Hausmann, 2009; Forget, 2010; Maze and Marshall, 2011; Maze et al., 2009). A first objective of our study has been to carry out similar diagnostics and draw comparable figures in a realistic eddy-resolving simulation. In this way we can assess the role of mesoscale eddies in EDW formation.

In our simulation, EDW occupies a coherent large scale structure located just south of the Gulf Stream, trapped between the seasonal and permanent thermoclines, as commonly described in observations – the so-called "bowl" of EDW. Nevertheless, while in observations the PV distribution over the outcrop of EDW is rather uniform and smooth (Maze and Marshall, 2011), the mesoscale imprint on the outcrop PV distribution is evident in the eddy-resolving simulation. This suggests that the structure of the EDW formation process is modulated by the oceanic mesoscale.

Two bowls of EDW are clearly seen in the simulation, with slightly warmer temperature and higher PV in the south westernmost bowl. This is consistent with observations (Kwon and Riser, 2004), but we brought it to clearer focus in our simulations: the location of the two bowls seems to be constrained by EKE.

The second objective of our study is to determine the respective role of buoyancy fluxes vs Ekman-driven convection in EDW formation. We employ a mapping technique of PV fluxes at the surface, similar to Maze and Marshall (2011), which selects PV fluxes in winter time that ventilate the core of EDW. In this eddy-resolving simulation, the contribution of mechanical PV fluxes is much smaller (at least one order of magnitude) than that of diabatic PV fluxes, a result which is similar to that obtained in coarse resolution data sets such as OCCA. Drawing further the comparison with OCCA, the map of the buoyancy contribution is very similar in the eddy-resolving simulation and in non-eddy resolving OCCA, which suggests that mesoscale eddies do not significantly influence the location where buoyancy fluxes induce EDW formation. On the other hand, the mesoscale eddy signature is clearly visible in the mechanical PV fluxes. Hence these two processes are not equally responsive to mesoscale eddies. Nevertheless, the net annual mechanical PV fluxes are very similar to those estimated in OCCA, suggesting mesoscale processes overall do not influence the mechanical contribution to EDW formation.

In the simulation, the mechanical PV fluxes are positive (leading to EDW formation) along the northern flank of the GS extending some 200 km south of it, while they are negative (leading to re-stratification of the upper ocean) in the vicinity of the southern flank of the GS. This suggests that considering the

GS as a straight-line density front is not a valid assumption in an eddy-resolving simulation. Rather, the simulation shows the GS as a tongue of water that is warmer and lighter than its surroundings. As a result, Ekman-driven convection leads to the formation of EDW (i) along the northern flank of the GS as well as (ii) at the vertical of the EDW core bowl in the northern Sargasso Sea.

In this study, we have focused on evaluating surface fluxes of PV that contribute to EDW formation because it can be more readily evaluated in observational data sets. Understanding the full EDW dynamics and how mesoscale eddies influence it, via the 3-dimensional Bernoulli function as done in Maze and Marshall (2011) for instance, will be the subject of further study.

Acknowledgments

The authors are grateful to G. Madec for insightful discussions on Ekman layer representation in NEMO. Guillaume Maze was co-funded by the GIS Europole Mer, Ifremer and the CREST Argo project from the CPER Bretagne 2008–2013. The CREST Argo project is funded by Europe through the FEDER program and by the Brittany Region, Brest Metropole Oceane and CG29. John Marshall acknowledges support from NSF through the CLIMODE and MOBY projects.

References

Barnier, B., Madec, G., Penduff, T., Molines, J., Treguier, A., Le Sommer, J., Beckmann, A., Biastoch, A., Böning, C., Dengg, J., et al., 2006. Impact of partial steps and momentum advection schemes in a global ocean circulation model at eddy-permitting resolution. Ocean Dyn. 56 (5), 543–567.

Bates, N., Pequignet, A.C., Johnson, R.J., Gruber, N., 2002. A variable sink for atmospheric CO_2 in subtropical mode water of the north atlantic ocean. Nature 420, 489–493.

Boccaletti, G., Ferrari, R., Fox-Kemper, B., 2007. Mixed layer instabilities and restratification. J. Phys. Oceanogr.

Brodeau, L., Barnier, B., Treguier, A.M., Penduff, T., Gulev, S., 2010. An era40-based atmospheric forcing for global ocean circulation models. Ocean Model. 31, 88–104.

Bryan, F.O., Hecht, M.W., Smith, R.D., 2007. Resolution convergence and sensitivity studies with north Atlantic circulation models. Part 1: the western boundary current system. Ocean Model. 16, 141–159.

Chelton, D.B., DeSzoeke, R.A., Schlax, M.G., El Naggar, K., Siwertz, N., 1998. Geographical variability of the first baroclinic Rossby radius of deformation. J. Phys. Oceanogr. 28, 433–460.

Czaja, A., Frankignoul, C., 2002. Observed impact of Atlantic SST anomalies on the North Atlantic oscillation. J. Clim. 15 (6), 606–623.

Czaja, A., Hausmann, U., 2009. Observations of entry and exit of potential vorticity at the sea surface. J. Phys. Oceanogr. 39 (9), 2280–2294.

Dai, A., Trenberth, K.E., 2002. Estimates of freshwater discharge from continents: latitudinal and seasonal variations. J. Hydrometeorol. 3, 660–687.

Eden, C., Dietze, H., 2009. Effects of mesoscale eddy/wind interactions on biological new production and eddy kinetic energy. J. Geophys. Res. 114 (C5).

Fichefet, T., Morales Maqueda, M.A., 1997. Sensitivity of a global sea ice model to the treatment of ice thermodynamics and dynamics. J. Geophys. Res. 102, 12609–12646.

Forget, G., 2010. Mapping ocean observations in a dynamical framework: a 2004–2006 ocean atlas. J. Phys. Oceanogr. 40 (6), 1201–1221.

Forget, G., Maze, G., Buckley, M., Marshall, J., 2011. Estimated seasonal cycle of north atlantic eighteen degree water volume. J. Phys. Oceanogr. 41 (2), 269–286.

Fox-Kemper, B., Ferrari, R., Hallberg, R., 2008. Parameterization of mixed layer eddies. Part i: theory and diagnosis. J. Phys. Oceanogr. 38 (6), 1145–1165.

Frankignoul, C., Kestenare, E., 2005. Observed Atlantic SST anomaly impact on the nao: an update. J. Clim. 18 (19), 4089–4094.

Fratantoni, P.S., Pickart, R.S., 2007. The western north Atlantic shelfbreak current system in summer. J. Phys. Oceanogr. 37 (10), 2509–2533.

Ganachaud, A., Wunsch, C., 2000. Improved estimates of global ocean circulation, heat transport and mixing from hydrographic data. Nature 408 (6811), 453–457.

Haynes, P., McIntyre, M., 1987. On the evolution of vorticity and potential vorticity in the presence of diabatic heating and frictional or other forces. Journal of the Atmospheric Sciences 44 (5).

Kwon, Y., Riser, S., 2004. North Atlantic subtropical mode water: a history of ocean-atmosphere interaction 1961–2000. Geophys. Res. Lett. 31, 20.

Large, W., Yeager, S., 2004. Diurnal to Decadal Global Forcing for Ocean and Sea-ice Models: The Data Sets and Flux Climatologies. NCAR Technical Note. Technical Report NCAR/TN-460+STR, 111 pp.

Large, W., Yeager, S., 2009. The global climatology of an interannually varying air–sea flux data set. Clim. Dyn. 33 (2), 341–364.

Le Sommer, J., Penduff, T., Theetten, S., Madec, G., Barnier, B., 2009. How momentum advection schemes influence current-topography interactions at eddy-permitting resolution. Ocean Model. 29, 1–14.

Levitus, S., Boyer, T.P., Conkright, M.E., O'Brian, T., Antonov, J., Stephens, C., Stathopolos, L., Johnson, D., Gelfeld, R., 1998. Noaa atlas nesdid. Technical Report.

Levy, M., Klein, P., Treguier, A.M., Iovino, D., Madec, G., Masson, S., Takahashi, K., 2010. Modifications of gyre circulation by sub-mesoscale physics. Ocean Model. 34, 1–15.

Madec, G., 2008. NEMO Ocean Engine. vol. 27. Note du Pole de Modelisation.

Madec, G., Imbard, M., 1996. A global ocean mesh to overcome the north pole singularity. Clim. Dyn. 12 (6), 381–388, http://dx.doi.org/10.1007/BF00211684.

Marshall, D.P., 2000. Vertical fluxes of potential vorticity and the structure of the thermocline. J. Phys. Oceanogr. 30 (12), 3102–3112.

Marshall, J., Adcroft, A., Hill, C., Perelman, L., Heisey, C., 1997a. A finite-volume, incompressible Navier–Stokes model for studies of the ocean on parallel computers. J. Geophys. Res. 102 (C3), 5753–5766.

Marshall, J., Andersson, A., Bates, N., Dewar, W., Doney, S., Edson, J., Ferrari, R., Forget, G., Fratantoni, D., Gregg, M., Joyce, T., Kelly, K., Lozier, S., Lumpkin, R., Maze, G., Palter, J., Samelson, R., Silverthorne, K., Skyllingstad, E., Straneo, F., Talley, L., Thomas, L., Toole, J., Weller, R., 2009. The climode field campaign: observing the cycle of convection and restratification over the gulf stream. Bull. Am. Meteorol. Soc. 90 (9), 1337–1350.

Marshall, J., Hill, C., Perelman, L., Adcroft, A., 1997b. Hydrostatic, quasi-hydrostatic, and nonhydrostatic ocean modeling. J. Geophys. Res. 102 (C3), 5733–5752.

Marshall, J., Jamous, D., Nilsson, J., 2001. Entry, flux and exit of potential vorticity in ocean circulation. J. Phys. Oceanogr. 31, 777–789.

Marshall, J., Nurser, J.G., 1992. Fluid dynamics of oceanic thermocline ventilation. J. Phys. Oceanogr. 22, 583–595.

Maze, G., Forget, G., Buckley, M., Marshall, J., Cerovecki, I., 2009. Using transformation and formation maps to study the role of air–sea heat fluxes in north atlantic eighteen degree water formation. J. Phys. Oceanogr. 39 (8), 1818–1835.

Maze, G., Marshall, J., 2011. Diagnosing the observed seasonal cycle of atlantic subtropical mode water using potential vorticity and its attendant theorems. J. Phys. Oceanogr. 41, 1986–1999.

Olsina, O., Wienders, N., Dewar, W.K., 2013. The climatology and variability of eighteen degree water potential vorticity forcing. Deep Sea Res. II 91, 84–95.

Penduff, T., LeSommer, J., Barnier, B., Treguier, A.M., Molines, J., Madec, G., 2007. Influence of numerical schemes on current-topography interactions in 1/4 degrees global ocean simulations. Ocean Sci. 3 (4), 508–524.

Reverdin, G., Niiler, P.P., Valdimarsson, H., 2003. North atlantic ocean surface currents. J. Geophys. Res. 108 (C1), 20.

Taylor, J.R., Ferrari, R., 2010. Buoyancy and wind-driven convection at mixed layer density fronts. J. Phys. Oceanogr. 40 (6), 1222–1242.

Thomas, L., Taylor, J.R., Ferrari, R., Joyce, T., 2013. Symmetric instability in the gulf stream. Deep Sea Res. II 91, 96–110.

Thomas, L.N., 2005. Destruction of potential vorticity by winds. J. Phys. Oceanogr. 35, 2457–2466.

Thomas, L.N., Ferrari, R., 2008. J. Phys. Oceanogr. 38, 2501–2518.

Thomas, L.N., Joyce, T.M., 2010. Subduction on the northern and southern flanks of the gulf stream. J. Phys. Oceanogr. 40 (2), 429–438.

Trenberth, K.E., Caron, J.M., 2001. Estimates of meridional atmosphere and ocean heat transports. J. Clim. 14, 3433–3443.

Valdivieso Da Costa, M., Mercier, H., Treguier, A.M., 2005. Effects of the mixed layer time variability on kinematic subduction rate diagnostics. J. Phys. Oceanogr. 35 (4), 427–443.

Worthington, L., 1959. The 18 water in the sargasso sea. Deep Sea Res. 5, 297–305.

Zhang, Y., Rossow, W.B., Lacis, A.A., Oinas, V., Mishchenko, M.I., 2004. Calculation of radiative fluxes from the surface to top of atmosphere based on isccp and other global data sets: refinements of the radiative transfer model and the input data. J. Geophys. Res. 109 (D19).